Experimental study of corner fires—Part I: Inert panel tests

Davood Zeinali*[,a], Steven Verstockt[b], Tarek Beji[a], Georgios Maragkos[a], Joris Degroote[a] and Bart Merci[a]

[a] *Department of Flow, Heat and Combustion Mechanics, Ghent University, EA03, Sint-Pietersnieuwstraat 41, 9000 Gent, Belgium*

[a] *Department of Electronics and Information Systems, Ghent University, Technologiepark Zwijnaarde 19, AA-tower, 9052 Zwijnaarde, Belgium*

* *Corresponding author: davood.zeinali@ugent.be*

Abstract

Corner fires are known to spread more intensely in comparison with single wall fires. In view of the challenges associated with prediction of such fire behavior, the fire growth in a corner configuration of Medium Density Fiberboard (MDF) panels is investigated to provide a set of experimental data, performing Single Burning Item (SBI) tests. First, though, test results with inert calcium silicate panels are discussed for three values of HRR (10, 30 and 55 kW), allowing to address the main physics involved. The experimental data for 30 kW, the default SBI HRR, is used for detailed discussion of the observations. The SBI testing methodology, materials, and set-up are described. The results of total Heat Release Rates (HRR) and Smoke Production Rates (SPR), as well as the panel temperatures and total heat fluxes at several characteristic locations are analyzed. Moreover, the puffing frequency of the corner fire is characterized thanks to Video Fire Analysis (VFA) of the experimental footage. Additionally, flame heights are discussed, including the concept of mirroring. A new correlation for mean flame height is introduced, using the hypotenuse of the triangle as characteristic length for

entrainment of air into the fire plume, and expressing that the flame height increases proportional to the square root of the fire heat release rate. The 30 kW propane burner of the standard SBI test is shown to feature a mean flame height of nearly 0.9 m and a puffing frequency of 2 ± 0.3 Hz, and an average total heat flux exceeding 44 kW/m^2 near the burner early on in the test. The completeness of the dataset is expected to be useful for testing and development of CFD codes for corner fire scenarios.

Keywords: corner fire, single burning item test, heat release rate, heat flux

1. Introduction

In fire safety problems, corner fire scenarios are often considered in flame spread scenarios [1] since fires spread more intensely in such a configuration in comparison with single wall fires. This is because the rate of mixing with ambient air in a corner fire plume is less than that of a free burning fire plume [2], leading to extended flame heights and high plume temperatures [3]. This causes the walls to heat up more effectively in a corner fire configuration. Reduction in radiation losses to the surroundings and also re-radiation among the walls are other influencing factors [4]. Accordingly, an accurate description of pyrolysis of combustibles and surface flame spread in such a configuration by means of pyrolysis codes and Computational Fluid Dynamics (CFD) software is of great interest to the fire safety community. Correspondingly, numerous tests have been conducted to study the behavior of fire in corner configurations and to obtain suitable data for evaluation of fire modeling codes in this area, as in [2, 5–12], often resembling ISO Room Corner tests [13].

The corner fire tests in our experimental campaign comprise several Single Burning Item (SBI) tests [14]. From an experimental perspective, SBI constitutes a key fire spread test since it forms the basis for classification of linings in Europe [15] and is an intermediate-scale test aiming to bridge the gap between bench-scale tests such as Fire Propagation Apparatus (FPA) tests [16] and full-scale tests such as ISO Room Corner tests [13]. Subsequently, being able to accurately predict the corner fire behavior in SBI is equally important and of interest [17, 18]. More specifically, as the results of a previous study suggest [12], predicting the global HRR evolution in modeling of a SBI corner fire is more challenging than for ISO Room Corner or Cone Calorimeter tests [19], showing higher sensitivity to the boundary condition at the backside of the walls. In this view, our experimental campaign focuses on the corner fire behavior in SBI experiments through several tests conducted with Medium Density Fiberboard (MDF) panels as well as inert calcium silicate panels. We monitor the fire behavior in the tests using cameras from two different angles and measure the evolution of panel temperatures, total Heat Release Rates (HRR) and Smoke Production Rates (SPR), as well as the total heat fluxes at the standard thermal attack calibration points of SBI [14]. In Part II [20], the results obtained for MDF panels are discussed. Here, we focus on all the details of the experimental methodology and set-up.

In the present work, the evolution of the panel temperatures is investigated via through-thickness temperature measurements at various locations over the burning panels. In addition, the evolution of temperatures at the backside of the burning walls is discussed. This is an essential component since it helps quantifying the heat losses from the backside. Earlier numerical

studies of corner fires have indicated the need for experimental quantification of this heat loss [12, 21] and have highlighted its significance when transitioning from the small scale of Cone Calorimeter tests [19] to larger scales of SBI tests [14] and ISO Room Corner tests [13]. To the best of the authors' knowledge, this has not been investigated experimentally in a systematic manner before. Another relevant subject is the level of symmetry of the thermal attack on the two panels. This is investigated in our study via analysis of the evolution of the through-thickness panel temperatures, and Video Fire Analysis (VFA) [22, 23]. Furthermore, the puffing frequency of the corner fire is characterized in order to provide experimental data for comparison with that of free burning fire plumes [24].

Tests with inert Calcium Silicate (CS) panels are discussed, as in [5, 25–27]. The basic test ('CSCS') has the default SBI heat release rate of 30 kW. Two additional tests have been performed for HRR = 10 kW ('CSCS10kW') and 55 kW ('CSCS55kW'). While quantitatively obviously different, quantitatively no fundamental differences are observed. Therefore, the 30 kW results are used herein as the basis for the analysis of the phenomena observed.

2. Methods and materials

The material properties of the CS panels are presented in Table 1, as obtained from the technical specification sheet provided by the supplier. The general experimental set-up of the SBI tests has been previously described by the authors in [28]. Nevertheless, it is presented here in more detail. As portrayed in Fig. 1, two test panels are placed in a vertical position and

perpendicular to each other to form a corner. The *long panel* is 1.5 m high and 1.0 m wide, while the *short panel* is 1.5 m high and 0.5 m wide. The sample panels are conditioned prior to the tests at 21^oC and 50% relative humidity. A triangular propane sandstone burner with side dimension of 0.25 m is located at a 0.04 m clearance from the panels. The propane burner operates by default at a HRR of 30 kW, representing a corner fire source at the bottom corner of the panels. When the burner is ignited at the beginning of the experiments ($t = 0$ s), it takes less than 30 s for the burner to stabilize within ± 1 kW of the desired peak HRR (see Fig. 2), except in the case of 55 kW where it takes approximately 60 s.

The hood on top of the testing trolley extracts the gases at an average flow rate of 0.6 Nm^3/s (normal cubic meter per second at 298 K). Subsequently, the evolution of the total HRR and SPR is determined based on the concepts of oxygen depletion [29] and smoke obscuration [30], respectively.

Table 1: material properties of the CS panels (from the source supplier)

Property	**Value**
Thickness [m]	0.0123 ± 0.001
Density [kg/m^3]	$1005 \pm 5\%$
Moisture content [%]	5 - 10
Thermal conductivity [W/(m.K)]	0.17^{a}
Specific heat capacity [J/(kg.K)]	920^{b}

^{a} The nominal value of thermal conductivity is 0.17, 0.19 and 0.21 W/(m.K) at temperatures of 293, 373 and 473 K.

^{b} The nominal value at 673 K.

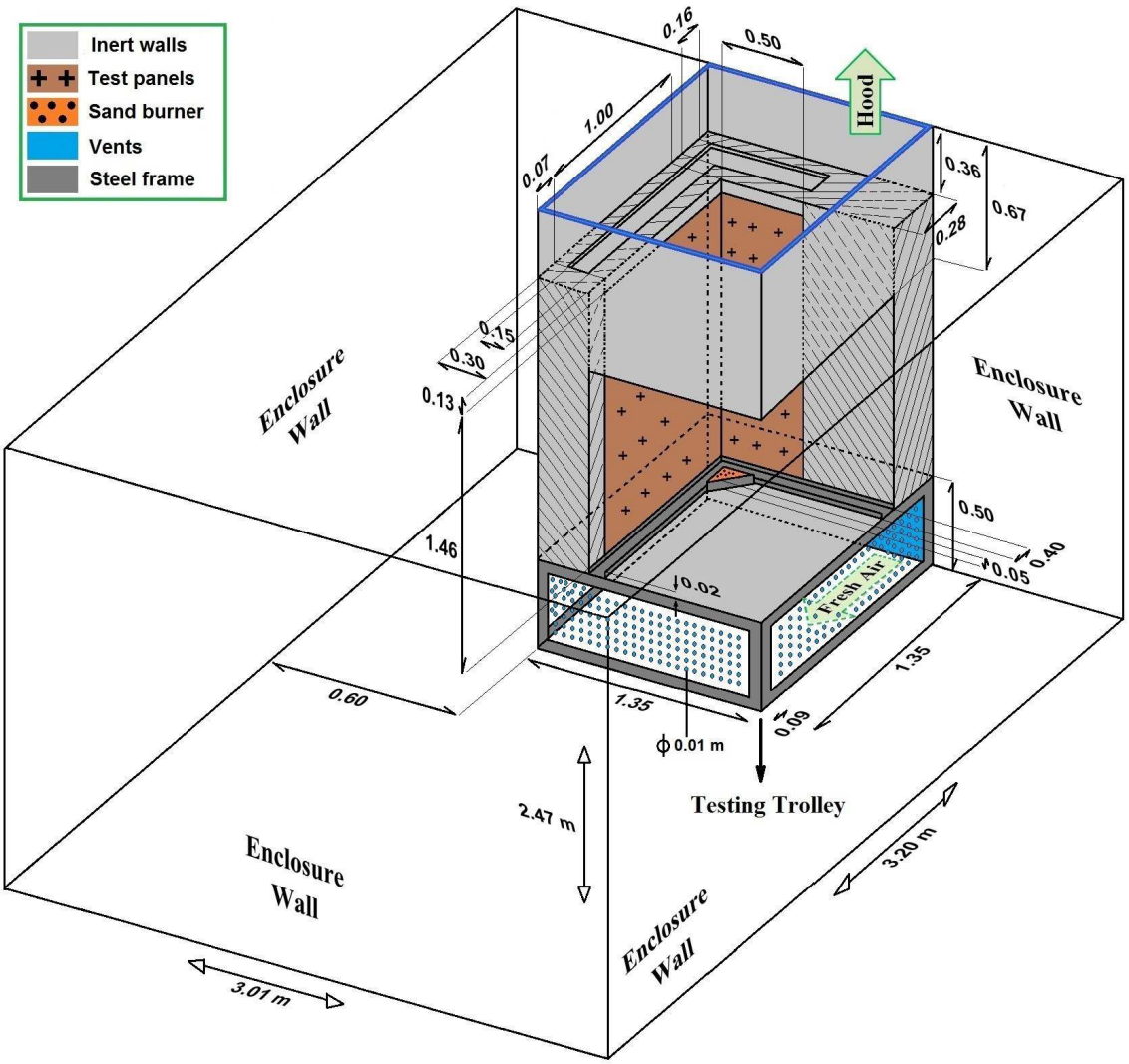

Figure 1: The geometry of the SBI tests' enclosure (units in m): there are two openings in the enclosure, namely the hood on top of the testing trolley, which extracts the gases (0.6 Nm^3/s), and the vent at the bottom of the backside of the trolley (1.16 m by 0.32 m) where fresh air enters the enclosure. The bottom sides of the trolley are covered with perforated steel plates (50% open area), to produce a more uniform airflow. The total exposed height of the panels is 1.46 m, and there is an air gap behind each panel, i.e., 0.30 m wide behind the long panel and 0.28 m wide behind the short panel. The image is not to scale.

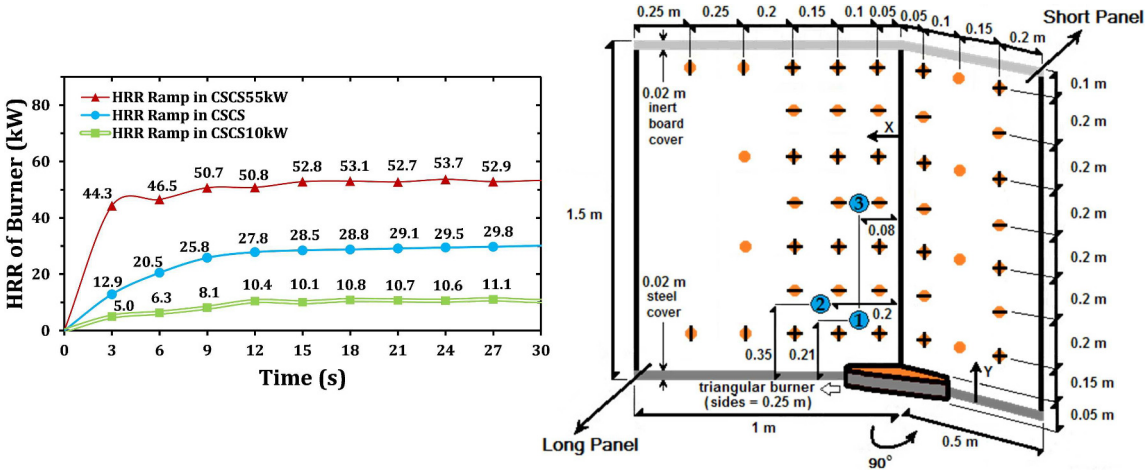

Figure 2: The HRR ramp of the burner at the start of the SBI tests (to the left), and the layout of the measurements made on the panels in the SBI experiments (to the right, with distance units in meters): panel temperatures are measured using thermocouples either at 0.001 m depth only (●), at 0.001 m depth and the backside (◗), at 0.001 m and 0.002 m depth (⬬), or at 0.001 m, 0.002 m and the backside simultaneously (✚). Total heat fluxes are measured using sensors ① to ③ . Horizontal and vertical axes references have been denoted with X and Y, respectively. The right drawing is not to scale.

Temperature measurements are made all over the panels at different depths and at the backside using K-type thermocouples, as depicted in Fig. 2. The through-thickness measurements are made by placing the thermocouples inside holes, drilled from the backside of the panels. Conduction along the thermocouple-leads is assumed to be negligible. Each thermocouple has its wires welded only at one terminal bead to ensure that through-thickness temperatures are recorded strictly at the desired depth. The thermocouple bead, sized approximately 0.0015 m, is fixed in place firmly using thermal adhesive 940 HT-1 from Polytec PT in Germany. This paste provides superior thermal conductivity (with thermal conductivity of 2.1 W/(m.K), i.e. over

10 times that of the CS panels). Due to its alumina oxide base, the paste does not decompose at high temperatures and is electrically nonconductive so it does not interfere with the functioning of the thermocouples. For different depth measurements at the same location, independent holes are considered with 0.01 m separations, in order to reduce the influence from the neighboring measurements, and to have better contact between the thermocouple beads and the panel. It is illustrated below that this shift in position is not crucial for the temperature evolutions (Fig. 10).

Measurements of total heat fluxes are made using water-cooled Schmidt-Boelter heat flux sensors with a working range up to 75 kW/m^2. As depicted in Fig. 2, the measurements are made at the three thermal attack calibration points set forth by Annex D.2 of SBI's standard [14]. As the combustion of propane from the burner yields a considerable amount of water vapor, condensation occurs on the cooled sensors, causing errors reported as high as 8% [10]. Therefore, as a conventional practice, the temperature of the cooling water supplied to the sensors is maintained at 50^oC to diminish condensation errors. All the sensors are set flush with the surface of the panels. Furthermore, the flame position is recorded by video cameras from two different angles, one facing the long panel and the other one facing the short panel.

3. Results and discussion

3.1. Heat Release Rates (HRR) and Smoke Production Rates (SPR)

The HRR and SPR evolutions, shown in Fig. 3, are determined as described in EN 13823 [14]. The HRR reaches the nominal value in approximately 30 s and has a very gradual rise until the end of the test. For test

CSCS, the average HRR during the final 100 s of the test is 31.9 kW, with corresponding standard deviation of 0.4 kW. This is consistent with the stability requirement specified by SBI's standard [14], i.e., an average burner HRR of 30.7 $\pm$ 2 kW. In case of tests CSCS10kW and CSCS55kW, the average HRR during the final 100 s of the test is 11.4 and 54.7 kW, respectively, with corresponding standard deviations of 0.3 and 0.5 kW. Very similarly, the SPR reaches a nominal value (0.05 m^2/s in test CSCS) after approximately 30 s. Thereafter, the SPR rises very gradually, but it nearly doubles over a span of 1000 s. The average SPR value during the last 200 s of test CSCS is 0.097 m^2/s (0.03 and 0.11 m^2/s in tests CSCS10kW and CSCS55kW, respectively).

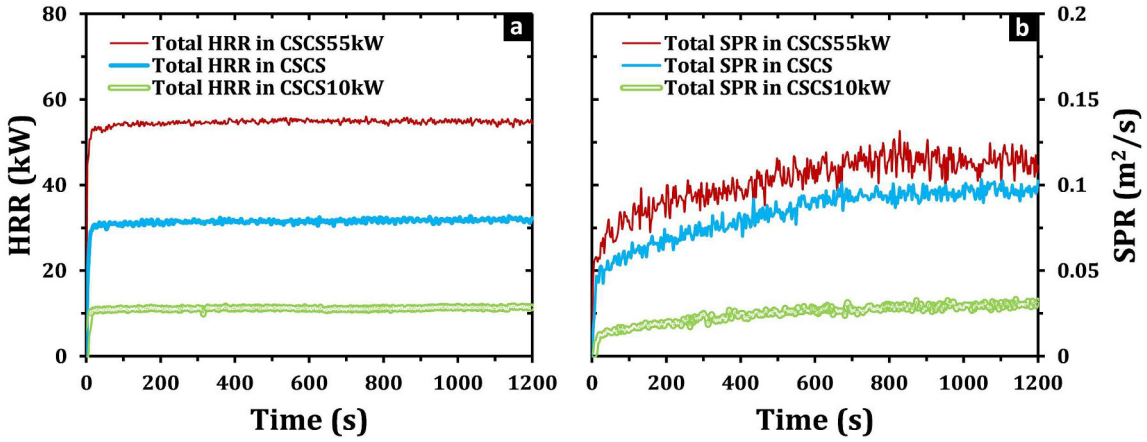

Figure 3: The evolution of total HRR (a) and SPR (b) for tests at 55 kW (CSCS55kW), 30 kW (CSCS) and 10 kW (CSCS10kW).

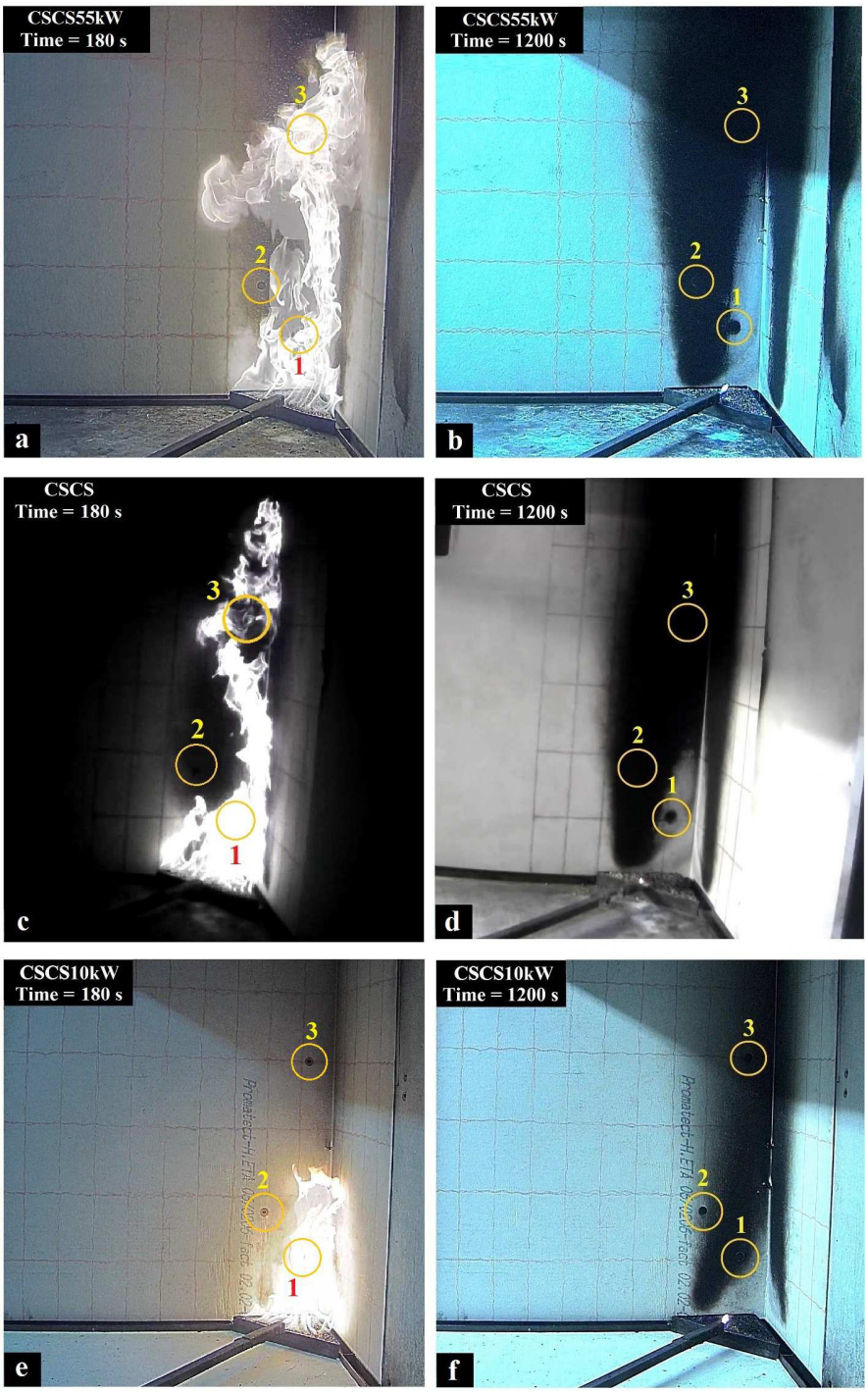

Figure 4: The flame shapes and soot deposition patterns on the CS panels in tests CSCS55kW (a and b), CSCS (c and d) and CSCS10kW (e and f): circles 1 to 3 indicate the heat flux sensors (located at positions shown in Fig. 2. Note that there is no soot deposition at the bottom corner.

The gradual rise in the HRR and SPR is expected to be due to the slow pyrolysis of the surface soot deposit on the CS panels (see Fig. 4). Figure 4 indicates no soot deposition on the panels at the bottom corner near the burner, suggesting more efficient combustion there, because the gas temperatures are the highest in that region. Note that this high temperature region is more extended at higher HRR as the soot deposition patterns suggest (Fig. 4). The gradual rise in the HRR and SPR profiles in Fig. 3 is not a 'drift' (i.e., a gradual increase in the measured value despite a constant physical value). The drifts associated with the measurements of gas concentrations (for HRR determination) and light attenuations (for SPR determination) are calculated after each test based on the specifications of SBI's standard [14] and are confirmed to be negligible.

3.2. Mean flame heights

The mean flame height is defined as the distance above the fire source where intermittency is 50% [31]. We retrieve the mean flame heights from the instantaneous flame heights from the experimental footage frames via software analysis [22, 23], averaging them over a window of 2 s, at every 20 s. The averaging window is limited to 2 s, equivalent to approximately 50-60 frames, to ensure minimal transient effects from the fire growth in case of fire spread (relevant for Part II [20]). The evolution of mean flame heights is presented in Fig. 5, along with corresponding data from Zhang et al. [17].

Zhang et al. [17] conducted 6 SBI tests with insulation fiberboard panels to determine the mean flame heights in the SBI configuration, at HHRs ranging from 15 to 60 kW. They measured the mean flame heights using an image processing technique based on the flame presence probability [32].

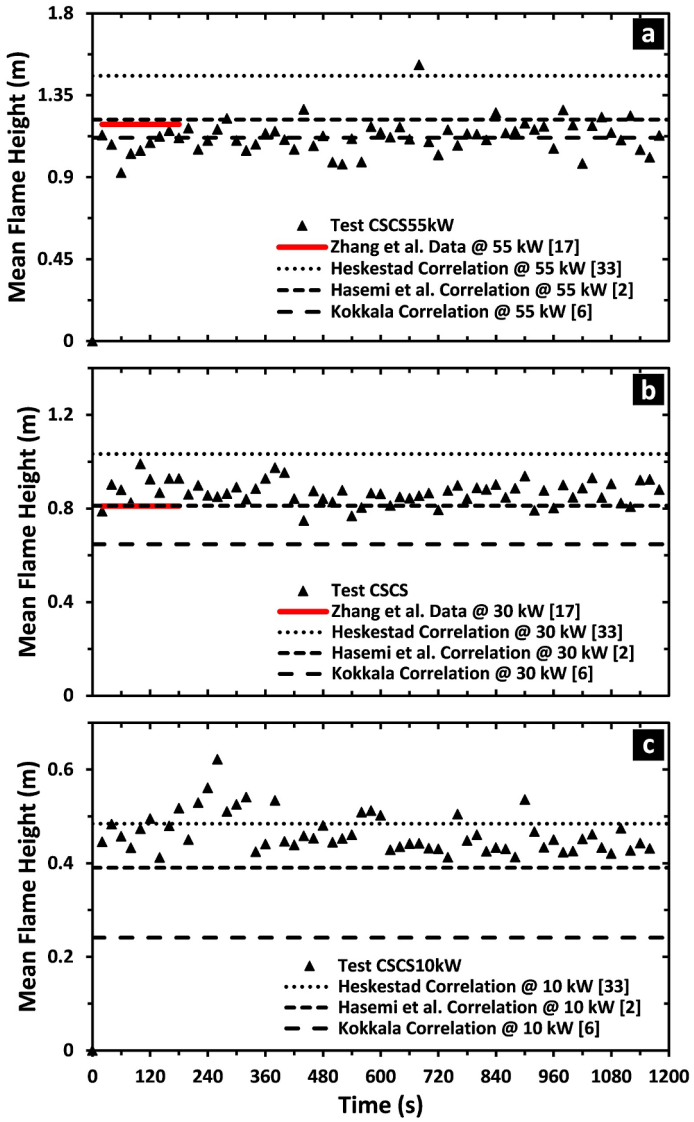

Figure 5: The mean flame heights for CSCS10kW (a), CSCS (b), CSCS55kW (c), along with corresponding data from Zhang et al. [17] and values from correlations of Hasemi et al. [2], Kokkala [6] and Heskestad [33], using the side length of the triangular burner as the characteristic fire diameter (refer to Eqs. 1 to 3).

Hence, they randomly selected a number of images from a footage sequence of approximately 180 s, and a flame height was obtained for each image. A probability was then associated with each obtained flame height, representing

its intermittency. Subsequently, the mean flame height was obtained where intermittency was 50%. As a result of this holistic approach, only one overall mean flame height was calculated for the entire 180 s of the footage in total. There is no value for 10 kW, but the values for 30 kW (0.81 m) and 55 kW (1.19 m) agree with our values to within 10%. The average mean flame heights in tests CSCS10kW, CSCS and CSCS55kW, are 0.46 m, 0.87 m, and 1.12 m, respectively.

It is worthwhile to analyze how the results compare to values obtained from existing correlations for corner fires. The following correlations are used, as expressed in Zhang et al. [17]:

- Hasemi et al. [2]: $H_{\text{f, avg}} = 3.65 \cdot D \cdot Q^{*2/3}$ (1)

- Kokkala [6]: $H_{\text{f, avg}} = 3.03 \cdot D \cdot Q^{*0.9}$ (2)

- Heskestad [33]: $H_{\text{f, avg}} = -2.04 \cdot D + 6.62 \cdot D \cdot Q^{*2/5}$ (3)

where $H_{\text{f, avg}}$ is the mean flame height (m), and Q^* is the dimensionless HRR parameter equal to $\dot{Q}/(\rho_a C_p T_a \sqrt{g} D^{5/2})$, where $\dot{Q}$ is the HRR (W), D is the characteristic fire diameter (m), and ρ_a, C_p and T_a are the density (kg/m^3), specific heat capacity (J/kg.K) and temperature (K) of the ambient air.

It must be noted that the correlations were developed based on square burners. Heskestad's correlation (Eq. 3) relies upon the assumption that a fire against a wall could be modeled as if there was an identical 'imaginary' fire mirrored on the other side of the wall. In the case of a corner configuration, the actual fire source is considered as one quarter of the total fire, i.e., actual plus imaginary (see Fig. 6.a). Thus, the flame height is determined as if the

total fire source burnt in the open air. This mirroring model is applicable for a corner fire only when the gap between the burner and the walls is less than twice the characteristic dimension of the burner [34], which is the case here (only 0.04 m distance from the corner).

As the correlations were originally not developed for triangular burners, it is not clear what is the 'best' fire diameter choice. The key physical phenomenon here is air entrainment from the sides. As such, the side length (0.25 m) of the triangle or the hypotenuse (0.35 m) are most strongly related to the physics involved. Yet, other geometrical choices are possible: equivalent diameter [35] ($\sqrt{4 \cdot A/P} = 0.2$ m), hydraulic diameter [36] ($4A/P = 0.15$ m), or square root of area [37] ($\sqrt{A} = 0.18$ m). Table 2 provides an overview of the results.

Another approach for estimating $H_{\text{f, avg}}$ would be to apply the mirroring principle for the triangular burner, starting from Heskestad's original correlation for a freely burning fire [33]:

$$H_{\text{f, avg}} = -1.02 \cdot D + 3.7 \cdot \left(\frac{1}{\rho_a C_p T_a \sqrt{g}} \right)^{2/5} \dot{Q}^{2/5} \tag{4}$$

Fig. 6.b makes clear that, in the case of a triangular burner, the length of the hypotenuse serves as D for the total fire, whereas $\dot{Q}$ is to be replaced by $4 \cdot \dot{Q}$ for the total fire (i.e., real corner fire plus imaginary source). Hence, for a triangular fire source in a corner, the correlation resulting from the mirroring principle should read:

$$H_{\text{f, avg}} = -1.02 \cdot D + 6.62 \cdot \left(\frac{1}{\rho_a C_p T_a \sqrt{g}} \right)^{2/5} \dot{Q}^{2/5} \tag{5}$$

Table 2: Mean flame heights obtained from correlations using different characteristic fire diameter definitions. The side length and hypotenuse are most directly related to the physics (air entrainment). Percentages indicate deviations from the experimental values (1.12 m for CSCS55kW, 0.87 m for CSCS and 0.46 m for CSCS10kW).

HRR (kW)	**Diameter definition**	**Prediction of correlation**		
		Hesami [2]	**Kokkala [6]**	**Heskestad [33]**
55	Side length (0.25 m) [17]	1.22 m (9%)	1.12 m (0%)	1.46 m (30%)
	Hypotenuse (0.35 m)	0.97 m (-13%)	0.73 m (-35%)	1.25 m (12%)
	Equivalent diameter (0.20 m) [35]	1.41 m (26%)	1.48 m (32%)	1.56 m (39%)
	Hydraulic diameter (0.15 m) [36]	1.74 m (55%)	2.18 m (95%)	1.67 m (49%)
	Square root of area (0.18 m) [37]	1.53 m (37%)	1.72 m (54%)	1.61 m (43%)
30	Side length (0.25 m) [17]	0.81 m (-7%)	0.65 m (-26%)	1.03 m (19%)
	Hypotenuse (0.35 m)	0.65 m (-25%)	0.43 m (-51%)	0.83 m (-5%)
	Equivalent diameter (0.20 m) [35]	0.94 m (9%)	0.86 m (-1%)	1.14 m (31%)
	Hydraulic diameter (0.15 m) [36]	1.16 m (33%)	1.26 m (45%)	1.24 m (43%)
	Square root of area (0.18 m) [37]	1.02 m (18%)	1.00 m (15%)	1.18 m (36%)
10	Side length (0.25 m) [17]	0.39 m (-15%)	0.24 m (-48%)	0.48 m (5%)
	Hypotenuse (0.35 m)	0.31 m (-32%)	0.16 m (-66%)	0.28 m (-39%)
	Equivalent diameter (0.20 m) [35]	0.45 m (-1%)	0.32 m (-31%)	0.59 m (28%)
	Hydraulic diameter (0.15 m) [36]	0.56 m (21%)	0.47 m (2%)	0.70 m (51%)
	Square root of area (0.18 m) [37]	0.49 m (7%)	0.37 m (-19%)	0.63 m (38%)

This correlation, unfortunately, tends to overestimate the mean flame heights (i.e., 0.64 m, 1.19 m, and 1.61 m, versus 0.46 m, 0.87 m and 1.12 m in tests CSCS10kW, CSCS and CSCS55kW, respectively). Interestingly, the experimentally determined mean flame heights relate more closely to $Q^{*1/2}$:

$$H_{\mathrm{f,\ avg}}/D = 4.0 \cdot Q^{*1/2} \tag{6}$$

with $R^2 = 0.9923$. This is in line with the correlation reported in [25] for the maximum flame heights of a square burner in a corner with a ceiling: $H_{\mathrm{f,\ max}}\ /D = 5.9 \cdot Q^{*1/2}$ (see Fig. 7).

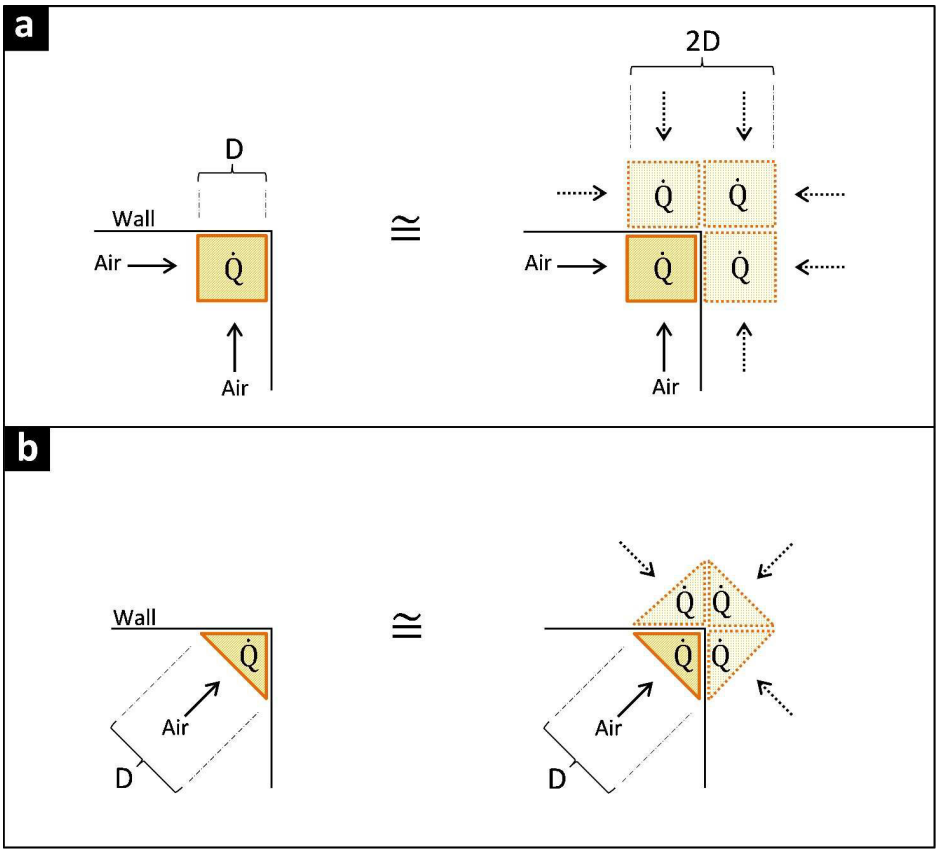

Figure 6: The mirroring model for estimating the mean flame height of a square burner in a corner [33] (top), and that advisable for the SBI triangular burner (bottom). Arrows indicate air entrainment sides, and parameters D and $\dot{Q}$ indicate the diameter and HRR of the burner, respectively. Refer to Eqs. 4 and 5 for explanations.

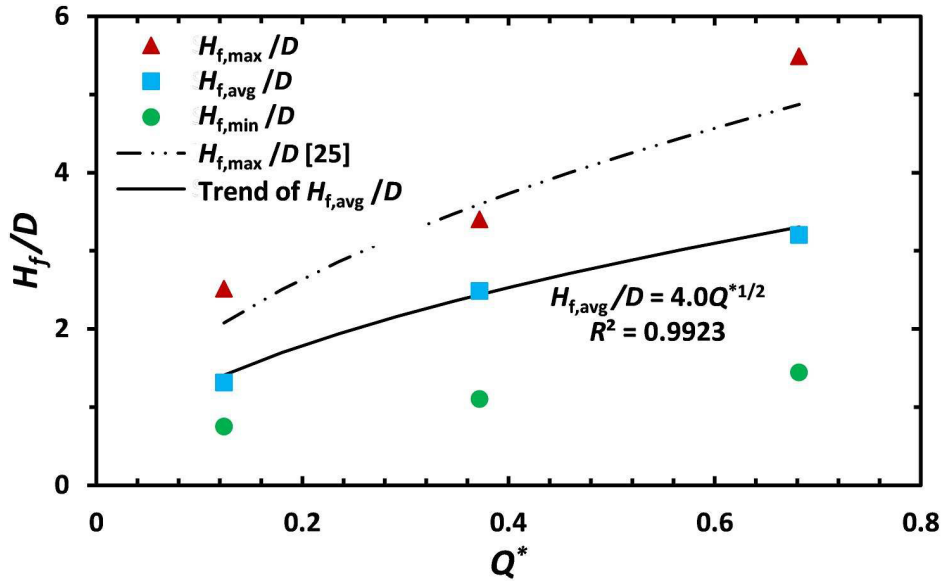

Figure 7: Dimensionless flame heights, $H_{\mathrm{f}}\ /D$, versus the dimensionless HRR parameter, $Q^* = \dot{Q}/(\rho_a C_p T_a \sqrt{g} D^{5/2})$, in tests CSCS10kW, CSCS and CSCS55kW, along with the correlation of Lattimer et al. [25] for $H_{\mathrm{f,\ max}}\ /D$ (note that they used a square burner in a corner with a ceiling). The characteristic diameter, D, is taken to be the hypotenuse of the SBI burner (0.35 m). Parameters $H_{\mathrm{f,\ min}}$, $H_{\mathrm{f,\ avg}}$ and $H_{\mathrm{f,\ max}}$, indicate the minimum, average and maximum flame heights, respectively.

3.3. Corner fire puffing frequency

Figure 8 shows the intermittency of the corner fire in test CSCS for a 1 s footage sequence between $t = 30$ and 31 s. This is when the flames from the burner are steady and there is no deposition of soot on the panels yet. As shown in Fig. 8, each second of the experimental footage contains several cycles of periodic 'puffing' [38], playing an important role in the heat release rate in the buoyant diffusion flames [39, 40].

The frequency of puffing is associated with the rate of air entrainment into the plume. For a freely burning flame with a round burner geometry,

entrainment is essentially the same from all directions. With a square burner geometry, there are some corner edge effects, although entrainment is still essentially the same from all the four sides. In the triangular geometry at hand, i.e., a right-angled triangle, the lengths of all the entrainment sides are not equal, and the corner edge effects are expected to be relatively large (i.e., the burner area is relatively small).

The puffing frequency has been evaluated for all tests by Fast Fourier Transform (FFT) analysis [41] of the flame heights after $t = 300$ s (Fig. 9). The sampling rate is 25 Hz and a total of $2^{11} = 2048$ samples are analyzed (sampling duration ≈ 82 s). The obtained puffing frequency values are roughly 2.2 Hz (CSCS55kW), 1.9 Hz (CSCS), and 2.0 Hz (CSCS10kW), respectively. Hence, there is no strong influence observable from the magnitude of HRR, just as reported in the literature [39, 40, 42]. Therefore, an approximate average value of 2 ± 0.3 Hz can be considered for the puffing frequency in tests CSCS55kW, CSCS, and CSCS10kW. Note must be taken that although the FFT amplitudes are occasionally high at frequencies near 0 Hz (Fig. 9), such low frequencies are not to be associated with the puffing phenomenon because their corresponding time-scale is several orders of magnitude longer than that relevant for puffing (expected in the range of 0.1 to 0.5 s for fire diameters between 0.1 and 0.5 m [42]).

The authors are not aware of other experimental data on puffing frequencies in corner configurations. Therefore, Table 3 shows a comparison with the correlation by Zukoski et al. [24], for free burning plumes:

$$f = (0.5 \pm 0.04) \cdot (g/D)^{1/2} \tag{7}$$

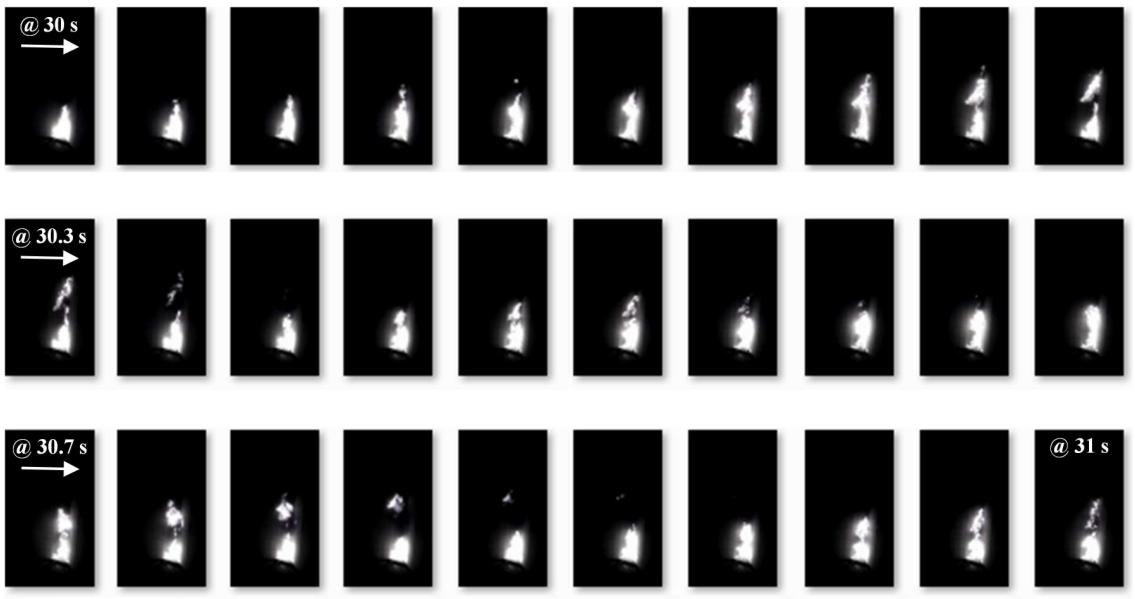

Figure 8: Corner fire intermittency in test CSCS during a sequence spanning $t = 30 - 31$ s: each second of the experimental footage contains several cycles of puffing [38].

where f is the puffing frequency (Hz), D is the fire diameter (m,) and g is the gravitational acceleration (9.81 m/s^2). The different options for D are used. As mentioned in Table 2, the side length and hypotenuse of the triangular burner are most directly related to the physics of air entrainment. The free plume puffing frequencies in Table 3 are reasonably higher than the average experimental value in tests CSCS55kW, CSCS and CSCS10kW, suggesting that puffing in the corner configuration is slower than that in open air configuration. This is expected since air entrainment is significantly restricted (by nearly 40% [43]), leading to slower puffing.

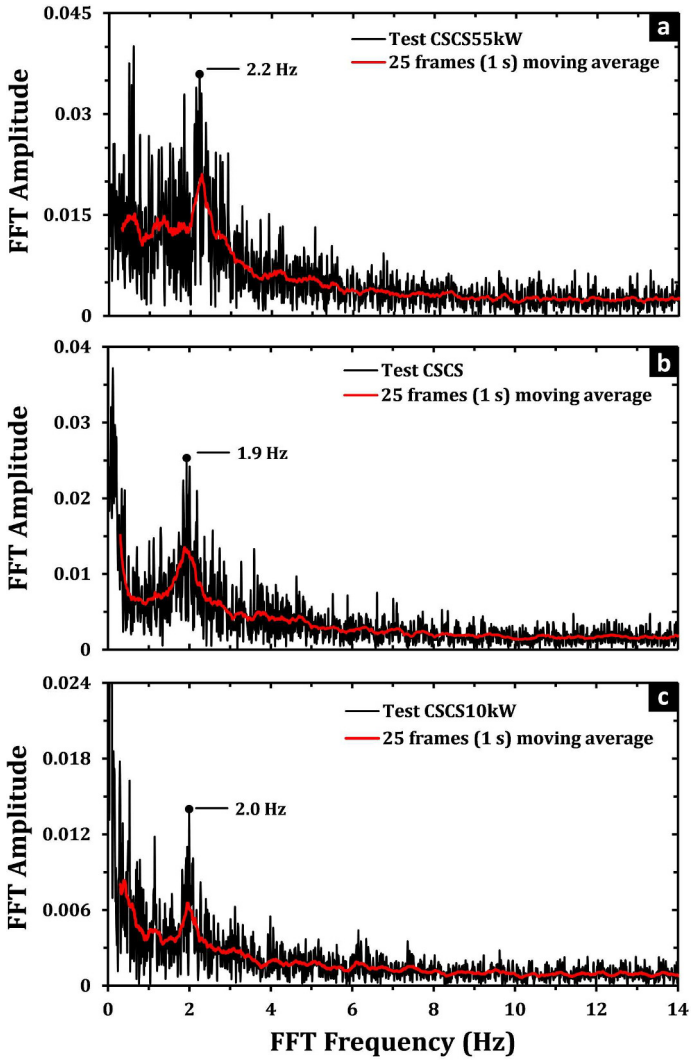

Figure 9: The puffing frequency for tests CSCS55kW (a), CSCS (b), and CSCS10kW (c), based on FFT analysis [41], with sampling rate = 25 Hz, and sampling duration = 82 s, i.e., $2^{11} = 2048$ samples.

Table 3: Free plume puffing frequencies obtained using the correlation of Zukoski et al. [24]. Note: this correlation was not developed for a triangular burner. The side length and hypotenuse are most directly related to the physics (air entrainment). Percentages indicate differences from the approximate average experimental value of 2 Hz observed for the corner fire puffing frequency in CSCS55kW, CSCS and CSCS10kW.

HRR (kW)	**Diameter definition**	**Free plume puffing frequency**
55, 30, or 10	Side length (0.25 m) [17]	3.1 ± 0.3 Hz (57 ± 13%)
	Hypotenuse (0.35 m)	2.6 ± 0.2 Hz (32 ± 11%)
	Equivalent diameter (0.20 m) [35]	3.5 ± 0.3 Hz (75 ± 14%)
	Hydraulic diameter (0.15 m) [36]	4.0 ± 0.3 Hz (102 ± 16%)
	Square root of area (0.18 m) [37]	3.7 ± 0.3 Hz (85 ± 15%)

4. Panel temperatures

As explained in section 2, panel temperatures are measured at 0.001 m and 0.002 m depth and at the backside. When multiple depth measurements are made at the same location, independent holes are drilled with 0.01 m 'separations' from each other. Fig. 10 reveals that this separation distance, either in vertical or horizontal direction, does not affect the measurements (only 4% average difference between the measurements at 0.002 m depth, while the distance between their corresponding thermocouples is $(0.01^2 + 0.01^2)^{0.5} \approx 0.014$ m). Note that Fig. 10 refers to the test with MDF panels (Part II [20]), which is more challenging than the CSCS tests here.

The patterns of the measured panel temperatures in test CSCS are shown as contour plots in Figs. 11 through 12, as well as temperature profiles in Figs. 13 through 16. The results for tests CSCS10kW and CSCS55kW are qualitatively very similar and have been uploaded on the online system of

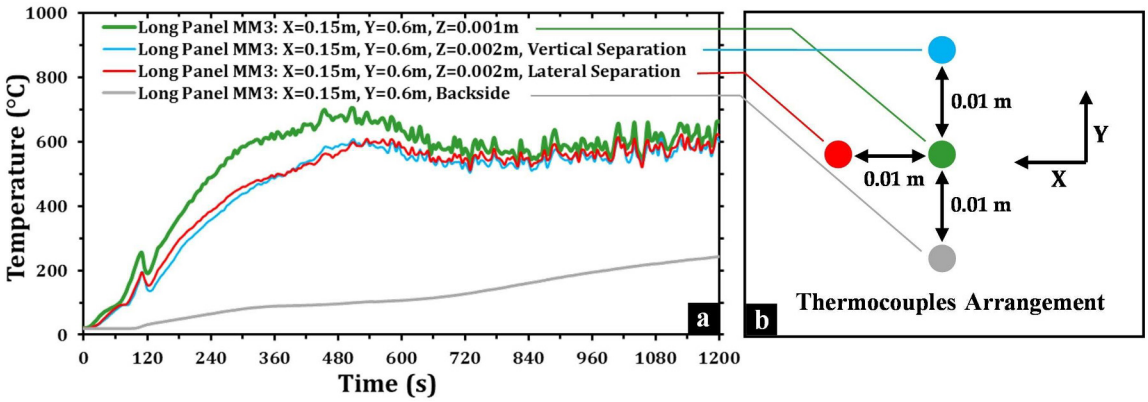

Figure 10: An example of different temperature evolutions recorded by thermocouples placed through the thickness and at the backside of the panels from test MM3 in Part II [20] (diagram 'a'), and the physical arrangement of the corresponding thermocouples (diagram 'b'): the measurements are made by allowing separations of 0.01 m between through-thickness and backside thermocouples. X and Y denote the distance from the corner and the bottom of the panels, respectively, while Z denotes the depth from the surface.

the journal as supplementary materials, containing videos that illustrate the evolution of panel temperature contour plots over the full duration of all the experiments. The contour plots in Figs. 11 through 12 are obtained by utilizing an interpolation scheme based on a combination of bilinear and polynomial least-square fitting using the QR matrix decomposition technique [44]. First, taking into account the known temperature values at the measurement points, optimal fitting polynomial functions are estimated of the form $aX^5 + bX^4 + cX^3 + dX^2 + eX + f$, where parameters a to f are constant coefficients while X is the horizontal distance from the corner. This is done at every height where measurements have been made, i.e., every 0.2

m (see Fig. 2). In the next step, vertices are considered at every 0.05 m on the panels for the aforementioned particular heights and the corresponding vertex temperatures are determined using the polynomial functions determined in the previous step. Finally, using the known vertex temperatures, the temperatures in all other areas are estimated via bilinear interpolation in the vertical and horizontal direction. For the contour plots in Fig. 12 that denote the temperatures across the entire thickness of the panels, a logarithmic least-square fitting is implemented instead. This is deemed more suitable in this case because previous cone calorimeter experiments [45] indicate that the temperature gradient across the thickness is much larger in the vicinity of the surface than in the regions near the backside of the panel, hinting at an exponential temperature distribution across the thickness. The logarithmic least-square fitting is performed by taking into account the measured temperature values at 0.001 m and 0.002 m depth and the backside, considering logarithmic functions of the form $a \times LN(z) + b$, where a and b are constants, LN is the natural logarithm function, and z is the depth through the thickness of the panel. This is done at every height where measurements have been made. In the next step, vertices are considered at every 0.001 m across the thickness for the aforementioned particular heights and the corresponding vertex temperatures are determined using the logarithmic functions determined in the previous step. Finally, using the known vertex temperatures, the temperatures in all other areas are estimated via bilinear interpolation in the vertical and through-thickness direction.

According to the contour plots in Figs. 11 and 12, the heating up of the panels near the corner is most severe in the persistent zone of the flames,

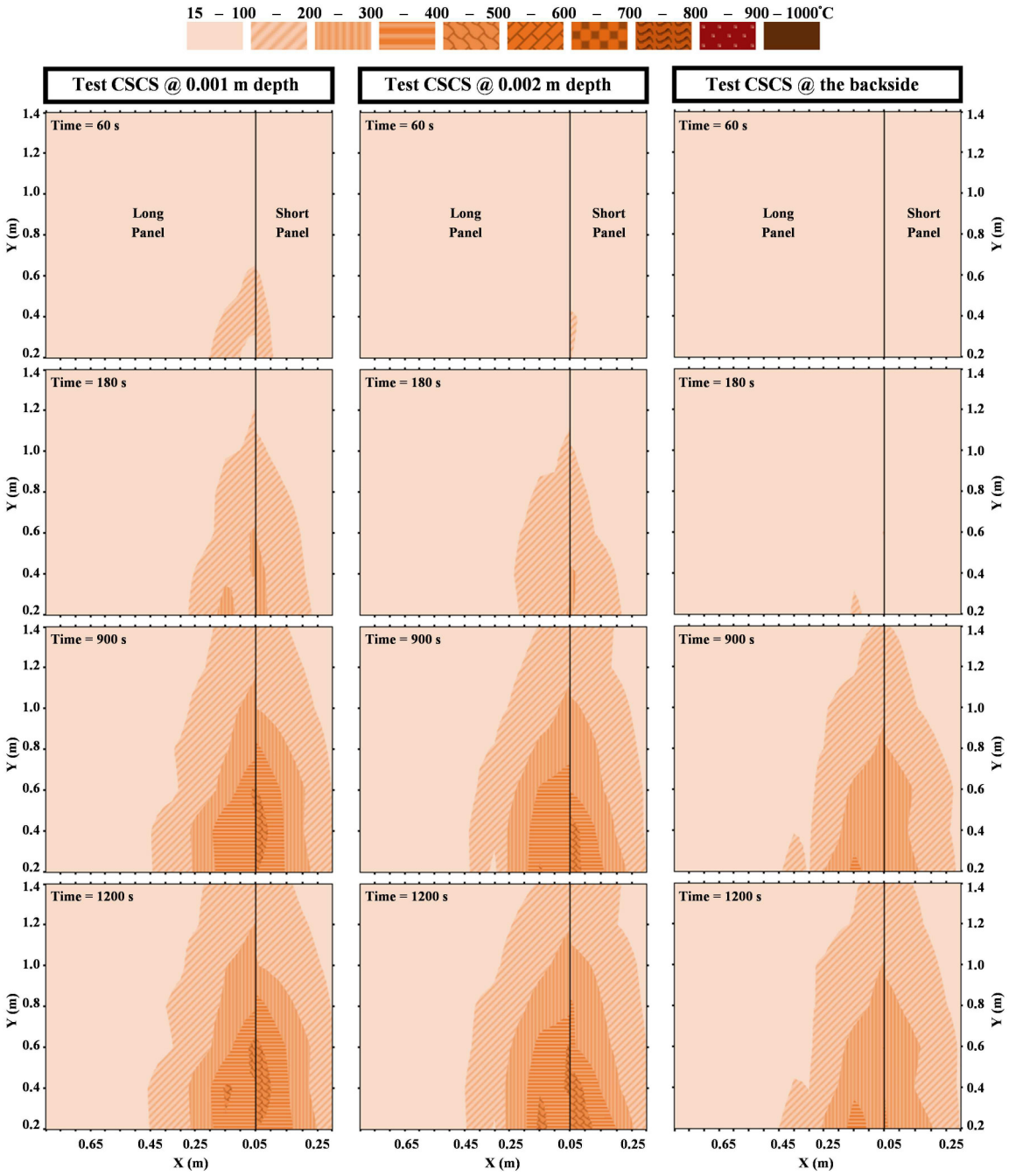

Figure 11: The evolution of the panel temperatures in test CSCS at 0.001 m depth (left column), at 0.002 m depth (middle column), and at the backside (right column): the X and Y axes denote the distance from the corner and the height from the bottom of the panels, respectively.

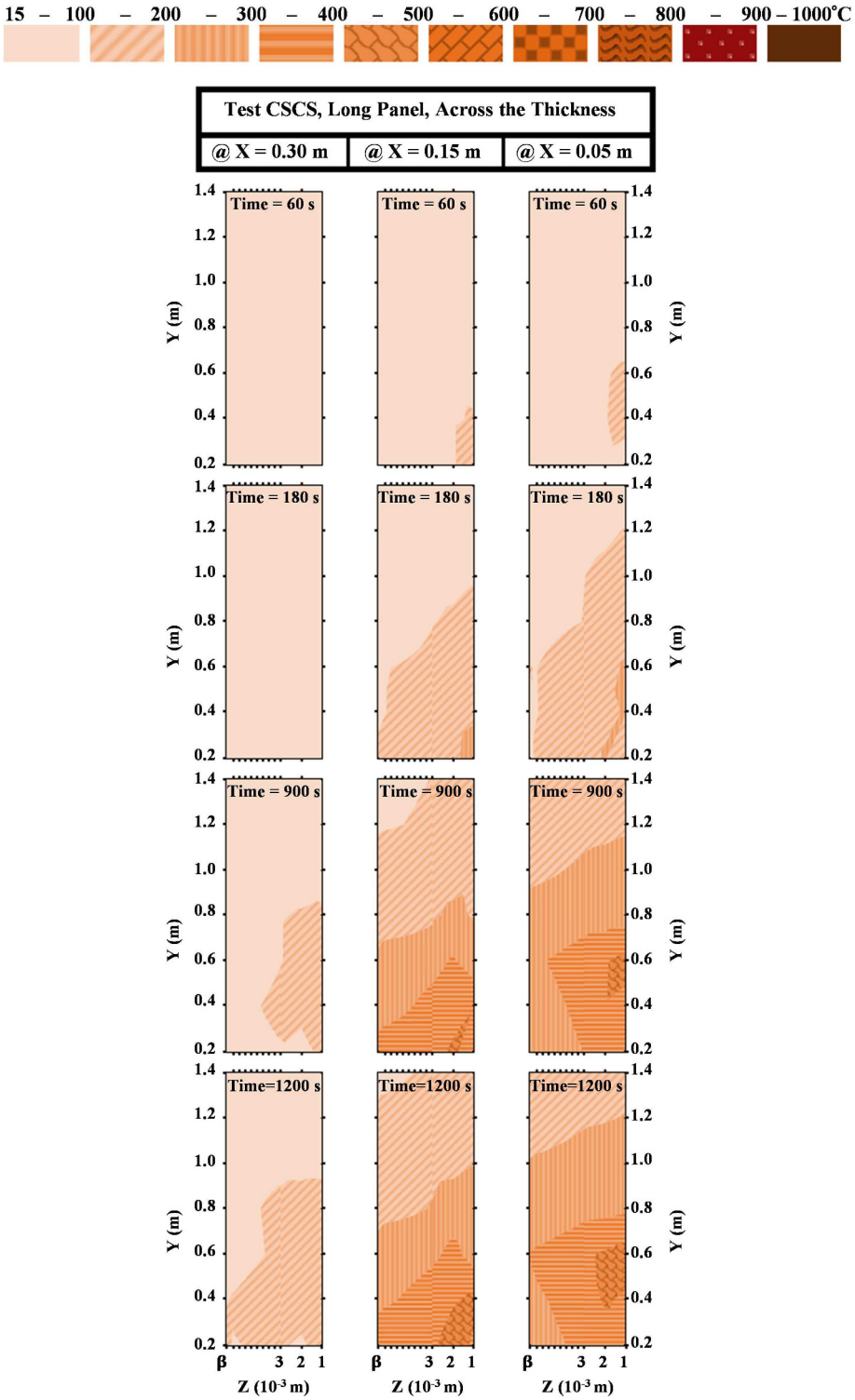

Figure 12: The evolution of temperatures across the thickness of the long panel at X = 0.3, 0.15 and 0.05 m in test CSCS: the X and Y axes denote the distance from the corner and the height from the bottom of the panels, respectively, while the Z axis denotes the depth through the thickness of the panel, with $\beta = 0.0123$ m representing the backside. The Z axis has been shrunken between 0.003 m and β linearly, for clarity.

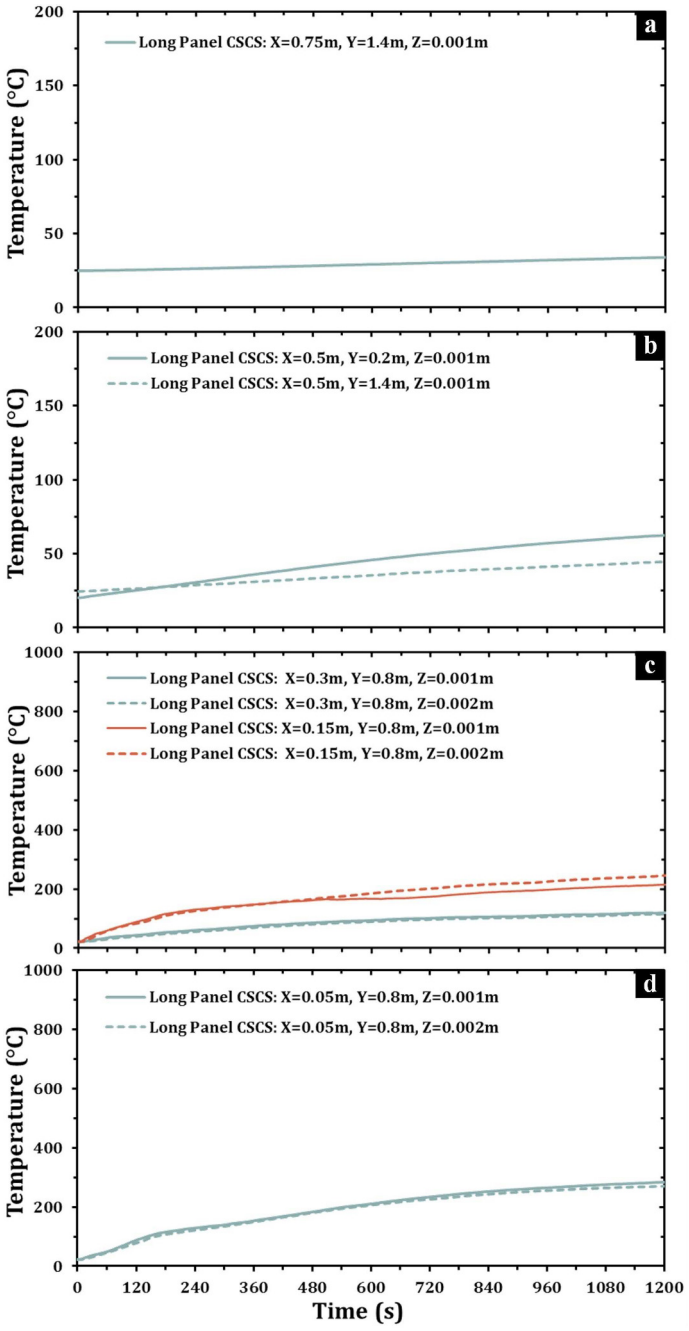

Figure 13: Long panel's through-thickness temperatures measured at different locations in test CSCS: X, Y and Z denote the distance from the corner, the distance from the bottom of the panels, and the depth from the surface, respectively.

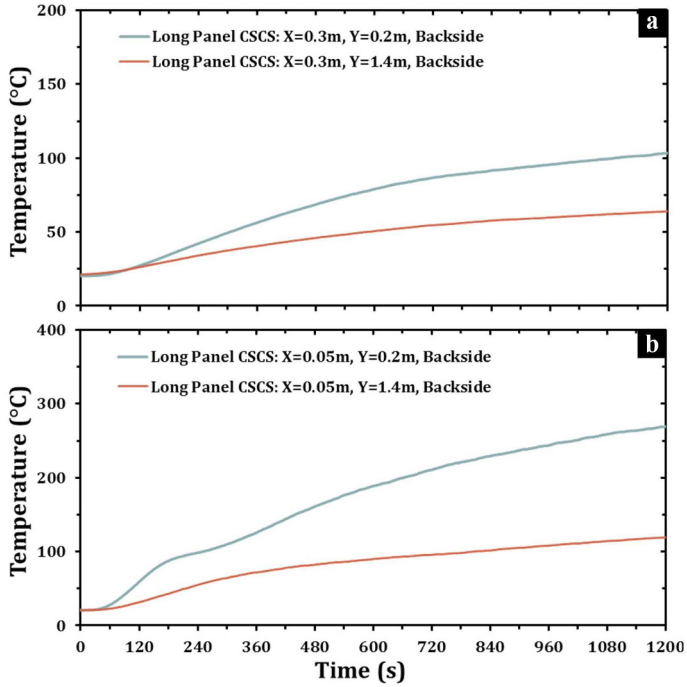

Figure 14: Long panel's backside temperatures measured at different locations in test CSCS: X and Y denote the distance from the corner, and the distance from the bottom of the panels, respectively.

particularly at heights between 0.4 and 0.6 m, with temperatures as high as 500^{o}C. This agrees with previous observations that the peak heat flux in the corner occurs where the continuous flame is attached to the walls [6, 25, 46]. Moreover, it is notable that the evolution of temperatures is slightly faster on the short panel near the burner. This is due to a set-up specific phenomenon. Zhang et al. [17] observed this in terms of slightly higher heat fluxes on the short panel, which they explained through air entrainment effects and the turbulent nature of the fire. Noting Fig. 8, it is appreciable that the air supplied from the bottom vent is initially directed more toward

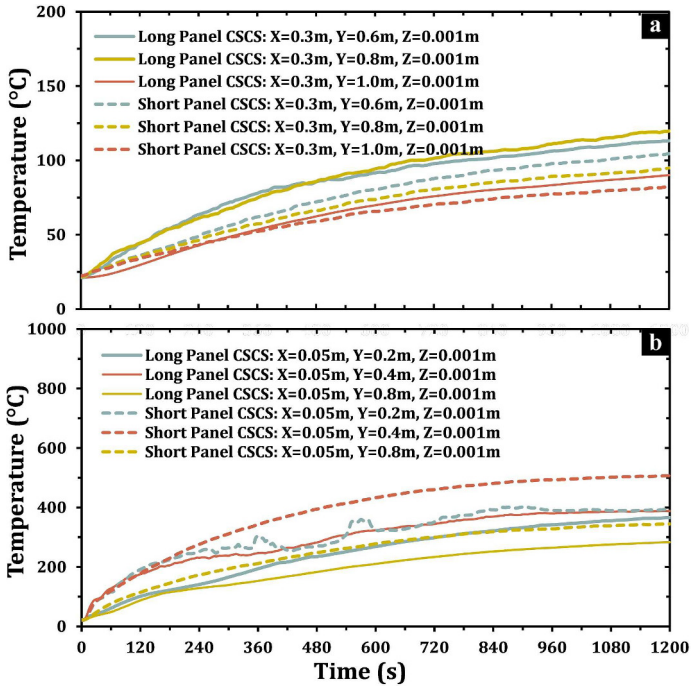

Figure 15: Comparison of long and short panels' measured through-thickness temperatures at different locations in test CSCS: X, Y and Z denote the distance from the corner, the distance from the bottom of the panels, and the depth from the surface, respectively.

the front side of the trolley, then flows back towards the short panel, and is eventually extracted by the hood. Thus, it is expected that the flames receive preferential air flow towards the short panel, leading to slightly stronger thermal attack near the burner on this panel.

At 0.55 m or further away from the corner, all the through-thickness and backside temperatures of the long panel remain below 100^{o}C (see contour plots in Fig. 11 and the temperature profiles in Fig. 13). A remarkable observation here is that the through-thickness temperatures within this zone start increasing as early as about $t = 60$ s whilst there are no flames present in this region. This early temperature rise is caused by the radiation received from the corner fire.

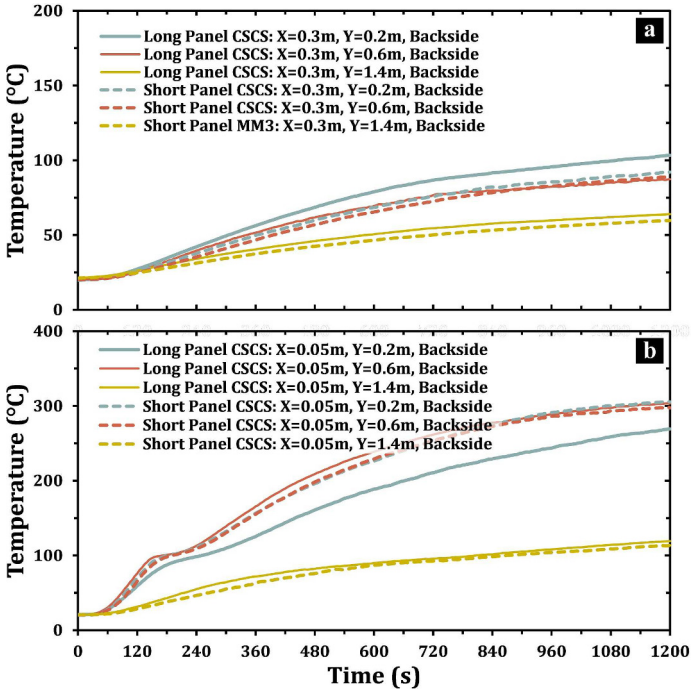

Figure 16: Comparison of long and short panels' measured backside temperatures at different locations in test CSCS: X, Y and Z denote the distance from the corner, the distance from the bottom of the panels, and the depth from the surface, respectively.

Near the corner, the pattern of some of the through-thickness panel temperatures features a momentary level-off before reaching 100^{o}C (Figs. 13.d, 14.b and 16.b). This level-off is due to the energy required to evaporate any moisture content trapped within the CS panels.

Backside panel temperatures near the corner start rising as early as 60 s (note temperature profiles in Fig. 14). This relates to the 'penetration time' [47], $t_p = (L^2 \cdot \rho \cdot C_p)/(16 \cdot k)$, where L is the thickness of the panels (m), ρ is the density (kg/m^3), C_p is the specific heat capacity (J/(kg.K)), and k is the thermal conductivity (W/m^2.K). Therefore, based on the material properties presented in Table 1, one can determine the corresponding penetration time of the CS panels as: $t_{p\,CS} = (0.0123^2 \times 1005 \times 920)/(16 \times 0.17) = 51s$.

5. Total heat fluxes

As the sensors were set flush with the surface of the panels and were in contact with hot gases or flames during the tests (Fig. 4), the measured fluxes are representative of total heat fluxes including radiative and convective heat exchanges [48, 49]. Since the flux measured by each sensor in the described conditions is primarily from radiation [50], it is essentially a function of a T^4 difference between the temperatures of the cooled periphery and the hot black core of the flux sensor. Consequently, although the temperature of the cooling water (set to 50^oC to avoid condensation, as explained in section 2) deviates from 20^oC (at which the sensors are calibrated), this has a negligible effect on the precision of the readings. As in a basic assessment [51], considering a black-body temperature of 1000^oC at the core of the sensor, and the 30^oC deviation of the temperature of the cooling water from 20^oC in the experiments, the ratio of the corresponding T^4 differences will be:

$$\frac{(1000+273)^4-(50+273)^4}{(1000+273)^4-(20+273)^4} \approx 0.9987 \tag{8}$$

which hints at a relative change of less than 0.13%, i.e. indeed insignificant. Nevertheless, there are typically various potential sources of uncertainty associated with this type of measurements, such as errors due to calibration and deposition of soot and dust, which generally lie below 10% [48, 50, 51]. As Bryant et al. [50] have recognized previously that one of the most influential errors is the change in the calibration constant, the heat flux sensors were recalibrated after each experiment to diminish this source of error. The calibration constant is a measure of the sensor's responsivity, and is calculated

by a linear regression fit to the sensor's output signal (in mV) for different known values of incident heat flux (in kW/m^2). After each SBI experiment, it was noticed that the calibration constant of the sensors remained within $\pm$ 3% of the initial calibration. Hence, the change in the responsivity of the sensors is very reasonable and lies within typical margins [51].

The total heat fluxes measured in tests CSCS55kW, CSCS and CSCS10kW are shown through Fig. 17 and Table 4. As expected, test CSCS55kW features the highest total heat fluxes for all the three sensors, while test CSCS10kW features the lowest heat fluxes. For all the sensors, the magnitude of heat flux difference between tests CSCS and CSCS10kW is over 100% more than that between tests CSCS and CSCS55kW. This is because as the total HRR is changed from 10 to 30 kW, the HRR increases by 200%, whereas a HRR change from 30 to 55 kW equals 83% increase in the HRR. The highest differences between tests CSCS and CSCS10kW are visible at the location of sensor 1 (located nearest to the burner), showing a difference of 29 kW/m^2 midway through the tests (Table 4). The corresponding difference between tests CSCS and CSCS55kW is only 8 kW/m^2. At the location of sensors 2 and 3, the total heat flux values are generally lower than those at the location of sensor 1, because these sensors are less frequently in the flame region (Fig. 4). This is more pronounced in test CSCS10kW, due to the smaller fire size (lower HRR) in this test.

All the measured total heat fluxes show a slight increase over the 1200 s of the experiment. This is mainly due to the gradual increase in the HRR (see Fig. 3) due to the slow pyrolysis of the surface soot deposit on the CS panels (see Fig. 4). Moreover, compared to a single wall fire, there is more

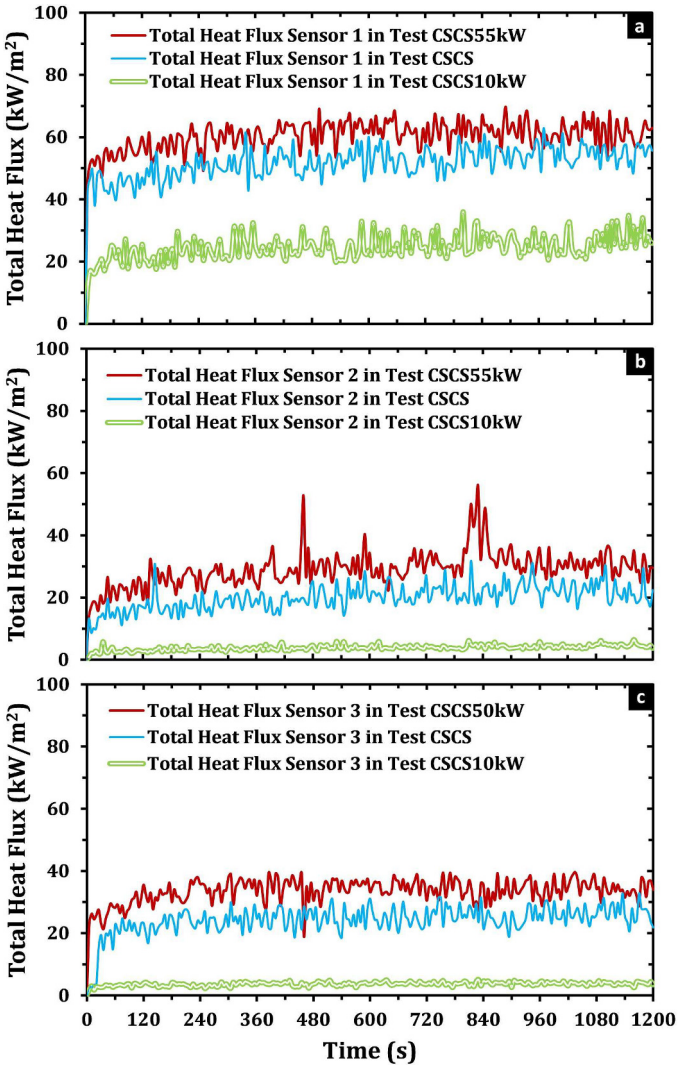

Figure 17: The total heat fluxes from sensors 1 to 3 in tests CSCS55kW, CSCS and CSCS10kW. The sensor locations have been shown in Fig. 2.

radiative heat exchange between the panels in a corner configuration (with higher view factor between the walls) [4], building up as the panels heat up over time. Therefore, the total heat fluxes on the panels increase over time as well. Furthermore, the deposit of soot on the panels causes a slight modification in the emissivity and absorptivity of the panels, although this

Table 4: Comparison of heat flux data from tests CSCS55kW, CSCS and CSCS10kW. Sensor locations: see Fig. 2.

Location	**Time**	**CSCS55kW**	**CSCS**	**CSCS10kW**
Sensor 1	t = 20 to 50 s	53 kW/m^2	44 kW/m^2	19 kW/m^2
	t = 600 to 630 s	63 kW/m^2	55 kW/m^2	26 kW/m^2
	t = 1140 to 1200 s	61 kW/m^2	55 kW/m^2	28 kW/m^2
Sensor 2	t = 20 to 50 s	34 kW/m^2	14 kW/m^2	3 kW/m^2
	t = 600 to 630 s	29 kW/m^2	20 kW/m^2	4 kW/m^2
	t = 1140 to 1200 s	30 kW/m^2	21 kW/m^2	5 kW/m^2
Sensor 3	t = 20 to 50 s	15 kW/m^2	16 kW/m^2	3 kW/m^2
	t = 600 to 630 s	35 kW/m^2	25 kW/m^2	4 kW/m^2
	t = 1140 to 1200 s	34 kW/m^2	26 kW/m^2	4 kW/m^2

is expected to have much less of an impact as the initial values of these two parameters are relatively high.

The total heat fluxes from test CSCS have been compared with corresponding data from a robin study by European Group of Official Laboratories for Fire Testing (EGOLF) [52], as well as the experimental study of Zhang et al. [17], through Fig. 18 and Table 5.

The EGOLF SBI round robin involved measurements from 10 different laboratories for the purpose of evaluating the repeatability and reproducibility of the thermal attack in SBI tests. Hence, every laboratory measured the total heat fluxes at the three locations shown in Fig. 2 during 300 s, for 5 times, and only the average of the results during the last 60 s was considered. The average total heat fluxes at the location of sensors 1, 2, and 3, were ap-

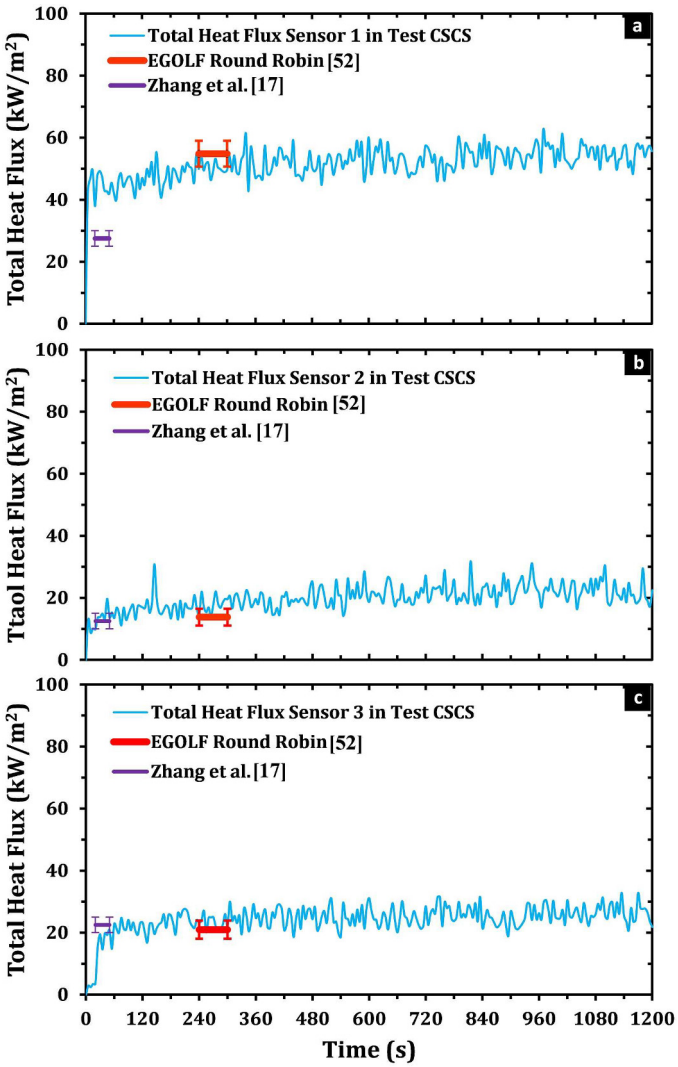

Figure 18: The total heat fluxes from sensors 1 to 3 in test CSCS in comparison with data from EGOLF round robin [52] and Zhang et al. [17]. The sensor locations have been shown in Fig. 2.

proximately 55, 14 and 21 kW/m^2, respectively. Zhang et al. [17] conducted 9 inert SBI tests with insulation fiberboard panels. They considered 3 HHRs, namely 30, 45 and 60 kW, each carried out for a duration of 60 s, for 3 times. A 30 s averaging window was considered for each experiment, and the av-

Table 5: Comparison of heat flux data from test CSCS with data from Zhang et al. [17] and EGOLF [52]. Sensor locations: see Fig. 2.

Location	**Test CSCS**	**Zhang et al. [17]**	**EGOLF [52]**
Sensor 1	44 kW/m^2 (t = 20 to 50 s) 50 kW/m^2 (t = 240 to 300 s)	25-30 kW/m^2 (t = 20 to 50 s) – – –	– – – 55 kW/m^2 (t = 240 to 300 s)
Sensor 2	14 kW/m^2 (t = 20 to 50 s) 18kW/m^2 (t = 240 to 300 s)	10-15 kW/m^2 (t = 20 to 50 s) – – –	– – – 14 kW/m^2 (t = 240 to 300 s)
Sensor 3	16 kW/m^2 (t = 20 to 50 s) 23 kW/m^2 (t = 240 to 300 s)	20-25 kW/m^2 (t = 20 to 50 s) – – –	– – – 21 kW/m^2 (t = 240 to 300 s)

erage of the 3 experiments was reported. Based on their final results at 30 kW HRR, the average total heat fluxes at the location of sensors 1, 2, and 3, were between 25 and 30 kW/m^2, between 10 and 15 kW/m^2, and between 20 and 25 kW/m^2, respectively.

The total heat fluxes measured in test CSCS align with the average values from the EGOLF SBI round robin (Fig. 18 and Table 5), with deviations of -9, 10 and 10% at locations 1, 2, and 3, respectively. The value of the total heat flux reported by Zhang et al. seems to be too low at location 1, i.e., immediately above the burner.

6. Conclusions

The corner fire characteristics in the SBI configuration were investigated with inert calcium silicate panels. The material properties, methodology and setup of the SBI tests have been presented. The results of total Heat Release Rates (HRR) and Smoke Production Rates (SPR), mean flame heights, corner fire puffing frequency, panel temperatures, as well as total heat fluxes at several characteristic locations were discussed for 3 levels of HRR: 10 kW, 30 kW (i.e., the default value for SBI), and 55 kW. The presented dataset

is expected to be useful for evaluation and development of CFD codes for corner fire scenarios.

The mean flame heights and positions of the flame tip were analyzed using Video Fire Analysis (VFA) of the footage. In addition, the puffing frequency of the corner fire was characterized. Different choices for the 'characteristic diameter' of the triangular burner can be made for use in the correlations for mean flame height, and this choice has a strong impact on the results. From a physical point of view (air entrainment), the length of the hypotenuse is the most logical choice. It is noted, though, that existing correlations have not been developed for triangular burners, and applying the mirroring principle for the triangular burner leads to overestimation of the mean flame heights. A new correlation has been introduced, using the length of the hypotenuse as characteristic length for entrainment of air into the fire plume, and expressing that the flame height increases proportional to the square root of the heat release rate of the fire (Eq. 6).

The backside panel temperatures were discussed as well, establishing the backside boundary condition. While very useful for CFD simulations, this had not been investigated experimentally before.

The 30 kW propane burner of the standard SBI test was shown to feature a mean flame height of nearly 0.9 m and an average total heat flux exceeding 44 kW/m^2 close to the burner early on in the test. At HRRs of 10 and 55 kW, the mean flame heights were approximately 0.5 and 1.1 m, and the initial total heat flux levels near the burner were over 19 and 53 kW/m^2, respectively. The average puffing frequency was determined not to be strongly influenced by the HRR, being approximately 2 ± 0.3 Hz for all the HRR tested. This frequency

was found to be lower than that of a free plume in open air configuration, namely due to the more restricted air entrainment in the corner geometry. [Note, though, that the free plume correlation used was not developed for a triangular burner.] The panel temperatures suggest that the thermal attack near the burner is slightly stronger on the short panel side due to the set-up specific flow field. This was observed by Zhang et al. in [17] in terms of total heat fluxes, as well as in Part II [20] with MDF panels.

Changing the HRR from 10 to 30 kW caused a significant increase in the total heat fluxes, yielding almost 30 kW/m^2 additional heat flux near the burner. Changing the HRR from 30 to 55 kW caused considerably less increase in the heat fluxes (only about 8 kW/m^2 additional heat flux near the burner). This aligned reasonably with the corresponding levels of HRR change, namely 200% vs 83% HRR increase, respectively. Additionally, the total heat fluxes at HRR of 30 kW align well with a round robin study for CSCS [52], with deviations of 10% and less.

Acknowledgments

This research has been funded by the Research Foundation Flanders (FWO-Vlaanderen, Belgium) under project number G004912N. Dr. Tarek Beji is a post-doctoral fellow of Research Foundation Flanders. The authors gratefully acknowledge the support of WFRGent NV for their eminent support with materials and equipment, and master's student Emma Vandemoortele who assisted with the conduction and processing of tests CSCS10kW and CSCS55kW.

References

[1] R.B. Williamson, N.A. Dembsey, Advances in assessment methods for fire safety, Fire Saf. J. 20 (1993) 15-38.

[2] Y. Hasemi, T. Tokunaga, Some Experimental Aspects of Turbulent Diffusion Flames and Buoyant Plumes from Fire Sources Against a Wall and in a Corner of Walls, Combust. Sci. Technol. 40 (1984) 1-18.

[3] D. Drysdale, Interaction of the Fire Plume with Compartment Boundaries, in: An Introduction to Fire Dynamics, John Wiley and Sons, Chichester, 2011, pp. 151-156.

[4] B. Merci, T. Beji, Fluid Mechanics Aspects of Fire and Smoke Dynamics in Enclosures, CRC Press, the Netherlands, 2016.

[5] B.Y. Lattimer, U. Sorathia, Thermal characteristics of fires in a combustible corner, Fire Saf. J. 38 (2003) 747-770.

[6] M.A. Kokkala. Characteristics of a Flame in an Open Corner of Walls. Proceedings of the 6th International Fire Conference; 1993; London, England: Interscience Communications Ltd. p. 13-29.

[7] Z. Yan, G. Holmstedt, CFD and experimental studies of room fire growth on wall lining materials, Fire Saf. J. 27 (1996) 201-238.

[8] C. Qian, Turbulent Flame Spread on Vertical Corner Walls, Department of Mechanical Engineering, University of Kentucky, Kentucky, US, 1995, pp. 161.

[9] R.B. Williamson, A. Revenaugh, F.W. Mowrer, Ignition Sources In Room Fire Tests And Some Implications For Flame Spread Evaluation, Fire Saf. Sci. 3 (1991) 657-666.

[10] B.T. Lee, Standard room fire test development at the National Bureau of Standards, in: T.Z. Harmathy (Ed.) Fire safety: Science and Engineering, American Society for Testing and Materials, Philadelphia, PA, 1985, pp. 29-44.

[11] J.B. Fang, Fire Buildup in a Room and the Role of Interior Finish Materials, National Bureau of Standards, Center for Fire Research, Washington, DC, 1975.

[12] J. Hietaniemi, S. Hostikka, J. Vaari, FDS Simulation of Fire Spread Comparison of Model Results with Experimental Data, VTT Building and Transport, Espoo, Finland, 2004.

[13] ISO-9705, ISO Room Corner (1993) International Standard - Fire Tests - Full-Scale Room Test for Surface Products, International Standards Organization (ISO), 1993.

[14] EN-13823, Reaction to Fire Tests for Building Products (2002) Building Products Excluding Floorings Exposed to the Thermal Attack By a Single Burning Item, European Standard, 2002.

[15] R. van Mierlo, B. Sette, The Single Burning Item (SBI) test method a decade of development and plans for the near future, HERON 50 (2005) 191-207.

[16] ISO-12136, Reaction to Fire tests Measurement of Material Properties Using a Fire Propagation Apparatus, International Standards Organization (ISO), Geneva, Switzerland, 2011.

[17] J. Zhang, M. Delichatsios, M. Colobert, Assessment of Fire Dynamics Simulator for Heat Flux and Flame Heights Predictions from Fires in SBI Tests, Fire Technol. 46 (2010) 291-306.

[18] B. Messerschmidt, P. Van Hees, U. Wickström, Prediction of SBI (Single Burning Item) test results by means of cone calorimeter test results, Interflam 99, Edinburgh, 1999.

[19] ISO-5660, Reaction-to-Fire TestsHeat Release, Smoke Production and Mass Loss RatePart 1: Heat Release Rate (Cone Calorimeter Method), International Standards Organization (ISO), 2002.

[20] D. Zeinali, S. Verstockt, T. Beji, G. Maragkos, J. Degroote, B. Merci, Experimental study of corner fires—Part II: Flame spread over MDF panels, Combust. Flame 189 (2018) 491-505, https://doi.org/10.1016/j.combustflame.2017.10.023.

[21] M. Hjohlman, P. Andersson, Flame Spread Modelling of Textile Products, SP Technical Research Institute of Sweden, Borås, Sweden, 2008.

[22] S. Verstockt, S. Van Hoecke, N. Tilley, B. Merci, B. Sette, P. Lambert, C.-F.J. Hollemeersch, R. Van de Walle, FireCube: A multi-view localization framework for 3D fire analysis, Fire Saf. J. 46 (2011) 262-275.

[23] T. Beji, S. Verstockt, R.V. de Walle, B. Merci, Global analysis of multi-compartment full-scale fire tests ('Rabot2012'), Fire Saf. J. 76 (2015) 9-18.

[24] E.E. Zukoski, Properties of fire plumes, in: G. Cox (Ed.), in: Combustion Fundamentals of Fire, Academic Press, London, England, 1995, pp. 101-219.

[25] B.Y. Lattimer, U. Sorathia, Thermal characteristics of fires in a non-combustible corner, Fire Saf. J. 38 (2003) 709-745.

[26] T.J. Shields, G.W.H. Silcock, A.Z. Moghaddam, M.A. Azhakesan, J. Zhang, A comparison of fire retarded and non-fire retarded wood-based wall linings exposed to fire in an enclosure, Fire Mater. 23 (1999) 17-25.

[27] B. Sundström, The Development of a European Fire Classification System for Building Products, Department of Fire Safety Engineering, Lund University, Sweden, 2007.

[28] D. Zeinali, T. Beji, G. Maragkos, J. Degroote, B. Merci. Experimental study of upward and lateral flame spread on MDF boards in corner configurations. 2nd European Symposium of Fire Safety Science; 2015; Nicosia, Cyprus. p. 35-40.

[29] M.L. Janssens, Measuring rate of heat release by oxygen consumption, Fire Technol 27 (1991) 234-249.

[30] B.A.-L. Östman, Smoke and Soot, in: V. Babrauskas, S.J. Grayson (Eds.), in: Heat Release in Fires, Taylor & Francis, 1990, pp. 233-250.

[31] M.M. Khan, A. Tewarson, M. Chaos, Combustion Characteristics of Materials and Generation of Fire Products, in: M.J. Hurley, D.T. Gottuk, J. Hall, J.R., K. Harada, E.D. Kuligowski, M. Puchovsky, J.L. Torero, J. Watts, J.M., C.J. Wieczorek (Eds.), in: SFPE Handbook of Fire Protection Engineering, NY: Springer, New York, 2016, pp. 1143-1232.

[32] L. Audouin, G. Kolb, J.L. Torero, J.M. Most, Average centreline temperatures of a buoyant pool fire obtained by image processing of video recordings, Fire Saf. J. 24 (1995) 167-187.

[33] G. Heskestad, Fire Plumes. In: DiNenno PJ (ed) SFPE handbook of fire protection engineering, 2nd edn., National Fire Protection Association, Quincy.

[34] W. Takahashi, O. Sugawa, , H. Tanaka, M. Ohtake, Flame And Plume Behavior In And Near A Corner Of Walls. Fire Saf. Sci. 5 (1997): 261-271.

[35] K. Hill, J. Dreisbach, Verification and Validation of Selected Fire Models for Nuclear Power Plant Applications, Volume 2: Fire Dynamics Tools (FDTS), U.S. Nuclear Regulatory Commission, Office of Nuclear Regulatory Research (RES), Rockville, MD: 2005 and Electric Power Research Institute (EPRI), Palo Alto, CA. NUREG-1824 and EPRI 1011999.

[36] A. Bejan, A.D. Kraus, Heat Transfer Handbook, Volume 1, John Wiley & Sons, 2003.

[37] D. Forschungsgemeinschaft, Numerical flow simulation II: CNRS-DFG collaborative research programme results 1998 - 2000, volume 75 of notes on numerical fluid mechanics and multidisciplinary design notes on numerical fluid mechanics, Springer Science & Business Media, 2001.

[38] W. M. G. Malalasekera, H. K. Versteeg, K. Gilchrist, A Review of Research and an Experimental Study on the Pulsation of Buoyant Diffusion Flames and Pool Fires, Fire Mater. 20:6 (1996) 261-271.

[39] E.E. Zukoski, B.M. Cetegen, T. Kubota, Visible structure of buoyant diffusion flames, Symposium (International) on Combustion, Volume 20, Issue 1, 1985, Pages 361-366, ISSN 0082-0784.

[40] B.M. Cetegen, E.E. Zukoski, T. Kubota, Entrainment and Flame Geometry of Fire Plumes, Report to Center for Fire Research, NBS, Daniel and Florence Guggenheim Jet Propulsion Center, California Institute of Technology, Pasadena, CA (August, 1982)

[41] K. R. Rao, Do Nyeon Kim, Jae Jeong Hwang, Fast Fourier Transform: Algorithms and Applications, Springer Science and Business Media, 2011.

[42] A. Hamins, J.C. Yang, T. Kashiwagi, An experimental investigation of the pulsation frequency of flames, Symposium (International) on Combustion, Volume 24, Issue 1, 1992, Pages 1695-1702.

[43] E.E. Zukoski, , T. Kubota, B. Cetegen, Entrainment in fire plumes, Fire Saf. J., 3 (1981), 107121.

[44] J.E. Gentle, QR Factorization, in: Numerical Linear Algebra for Applications in Statistics, Springer Science & Business Media, Berlin, Germany, 1998, pp. 95-97.

[45] S.R. Wasan, P. Van Hees, B. Merci, Study of pyrolysis and upward flame spread on charring materialsPart I: Experimental study, Fire Mater. 35 (2011) 209-229.

[46] Y. Hasemi, M. Yoshida, S. Takashima, R. Kikuchi, Y. Yokobayashi, Flame length and flame heat transfer correlations in corner-wall and corner-wall-ceiling configurations, Interflam 96: Proceedings of the Seventh International Fire Conference, Cambridge, 1996.

[47] D. Drysdale, Heat Transfer, in: An Introduction to Fire Dynamics, John Wiley & Sons, Ltd, 2011, pp. 35-82.

[48] W.M. Pitts, A.V. Murthy, J.L. de Ris, J.-R. Filtz, K. Nygård, D. Smith, I. Wetterlund, Round robin study of total heat flux gauge calibration at fire laboratories, Fire Saf. J. 41 (2006) 459-475.

[49] U. Wickström, Temperature Calculation in Fire Safety Engineering, Springer International Publishing, 2016.

[50] R. Bryant, C. Womeldorf, E. Johnsson, T. Ohlemiller, Radiative heat flux measurement uncertainty, Fire Mater. 27 (2003) 209-222.

[51] M. Bundy, A. Hamins, E.L. Johnsson, S.C. Kim, G.W. Ko, D.B. Lenhert, Measurements of Heat and Combustion Products in Reduced-Scale Ventilation-Limited Compartment Fires, National Institute of Standards and Technology, Gaithersburg, MD, 2007.

[52] V. Rumbau, E. Guillaume, A. Sainrat, EGOLF SBI Thermal Attack Measurements Round Robin 2, LNE-Trappes, ZA de Trappes-Élancourt, TRAPPES Cedex, France, 2005.